Research Article Vol. 40, No. 3 / March 2023 / Journal of the Optical Society of America A 583

Journal of the Optical Society of America A

OPTICS, IMAGE SCIENCE, AND VISION

# Metasurface-based triple-band beam splitter with large spatial separation at visible wavelengths

LIFEI WEI[1] AND HUAMAO HUANG[1,2,*]

[1]Engineering Research Center for Optoelectronics of Guangdong Province, School of Physics and Optoelectronics, South China University of Technology, Guangzhou, Guangdong 510640, China
[2]State Key Laboratory of Applied Optics, Changchun Institute of Optics, Fine Mechanics and Physics, Chinese Academy of Sciences, Changchun, Jilin 130033, China
*schhm@scut.edu.cn

Received 10 November 2022; revised 23 January 2023; accepted 29 January 2023; posted 30 January 2023; published 24 February 2023

**The dual-function of a wavelength beam splitter and a power beam splitter is desired in both classical optics and quantum optics. We propose a triple-band large-spatial-separation beam splitter at visible wavelengths using a phase-gradient metasurface in both the *x*- and *y*-directions. Under *x*-polarized normal incidence, the blue light is split in the *y*-direction into two equal-intensity beams owing to the resonance inside a single meta-atom, the green light is split in the *x*-direction into another two equal-intensity beams owing to the size variation between adjacent meta-atoms, while the red light passes directly without splitting. The size of the meta-atoms was optimized based on their phase response and transmittance. The simulated working efficiencies under normal incidence are 68.1%, 85.0%, and 81.9% at the wavelengths of 420 nm, 530 nm, and 730 nm, respectively. The sensitivities of the oblique incidence and polarization angle are also discussed.** 

https://doi.org/10.1364/JOSAA.480647

## 1. INTRODUCTION

A high-efficiency wavelength beam splitter, which is used to separate light beams with different wavelengths, is an important component in optical communications. For the separated wavelength, equal-intensity beams are required in both classical optics, such as in interferometry [1], and quantum optics, such as the generation of entangled photo light sources [2]. As a result, the cascaded device of a wavelength beam splitter and a power beam splitter is desired. Although one can realize the beam splitters by using many methods, including multiple-layer thin-films [3], coupled waveguides [4], optical gratings [5], and photonic crystals [6], the metasurface-based beam splitter has drawn remarkable attention because of its flexible optical wavefront manipulation and wavelength-scale size [7–38].

For a normal metasurface device, the different wavelength lights are redirected to different angles and form a rainbow beam. The wavelength dispersion can be estimated by the partial differential of the emergent angle with respect to the wavelength according to the generalized Snell's law [39]. In this way, the spatial separation of different wavelengths is limited, and thus the crosstalk between different wavelength channels would be high. A large spatial separation of dual-band wavelengths can be achieved by using a bilayer structure, in which each layer contains a metasurface to independently control the optical wavefront for a wavelength band [7–12]. A compact scheme is to integrate multiple patterns within a single layer, in which each pattern independently controls the optical wavefront for a wavelength band [13–24]. However, in these two schemes, the interval between the two wavelength bands should be large enough so that the second wavelength light can pass through the first metasurface with ignorable loss. Moreover, it is a great challenge for current nanofabrication technologies to prepare the meta-molecules with high accuracy in geometric dimensions and to align multiple patterns at a visible wavelength range. As a result, a metasurface having a simple structure for multiple-band wavelengths is attractive [25–28]. A dual-band beam splitter based on metal nano-bricks supporting gap-surface plasmon modes [25,26] or metal frustums supporting both grating modes and plasmonic modes [27] were proposed. The mechanism is that the orthogonal polarized lights at two discrete wavelengths are respectively controlled by the lengths of the meta-atom at two orthogonal directions [25,27] or that two discrete wavelengths are respectively controlled by two different order of plasmonic modes [26]. These metasurfaces with metal structure are reflective. A transmissive metasurface containing two identical silicon trapezoids with opposite directions was also proposed for a dual-band beam splitter [28]. The mechanism is also polarization-selective, which is the same as [25,27]. However, the spatial separation of the two wavelengths is small [28].

As for the power beam splitter, the design principle is to build the phase gradient along desired directions [29–38]. To achieve fine control, the multiple phase steps, in which the phase difference between adjacent meta-atoms is a fraction of $\pi$, should be

employed [29–35]. However, for the sake of compactness, the binary phase, in which the phase difference between adjacent meta-atoms is $\pi$, can be adopted [32–38]. The phase difference mainly comes from the different size [29,31,32,35–37], shape [33], or orientation [30,34] of the different meta-atoms. Within a single elongated rectangular meta-atom, the phase difference comes from the resonance along the $x$-direction for the $x$-polarized incident light [38].

To fulfill the requirement of compact minimization in a photonic device, a dual function of a wavelength beam splitter and a power beam splitter with large spatial separation and good working efficiency is desirable. In this paper, a transmissive metasurface having a simple pattern of a $TiO_2$ nano-brick array is proposed for a triple-band beam splitter, which is both a wavelength beam splitter and an equal-intensity power beam splitter, with large spatial separation at visible wavelengths. The blue light of 420 nm wavelength has equal-intensity splitting in the $y$-direction owing to the resonance inside a single meta-atom, the green light of 530 nm wavelength has equal-intensity splitting in the $x$-direction owing to the size variation between adjacent meta-atoms, while the red light of 730 nm wavelength passes directly without splitting, when the metasurface is illuminated by the three normal incident lights with $x$-polarization. The beam splitting angles in both the $x$- and $y$-directions obey the generalized Snell's law. The working efficiencies under normal incidence are 68.1%, 85.0%, and 81.9% at the wavelengths of 420 nm, 530 nm, and 730 nm, respectively. We believe our proposed method is useful for multiple channel communications.

## 2. DESIGN

The schematic diagram of our proposed triple-band large-spatial-separation beam splitter is shown in Fig. 1(a). The metasurface is composed of $TiO_2$ nano-bricks on a glass ($SiO_2$) substrate. An $x$-polarized triple-band plane wave is normally launched from a $SiO_2$ substrate and passes through the metasurface. The top view of the metasurface, which contains eight meta-atoms in the $x$-direction and seven meta-atoms in the $y$-direction, is illustrated in Fig. 1(b). Figure 1(c) shows the three-dimensional (3D) structure diagram of a single meta-atom. In the $x$-direction, a meta-molecule has an arrangement of meta-atoms in A-B-B-A style, in which A and B are two meta-atoms with different sizes. The phase of a green light in the meta-atom A is $\varphi_{x0}$ and that in the meta-atom B is $\varphi_{x0} \pm \pi$.

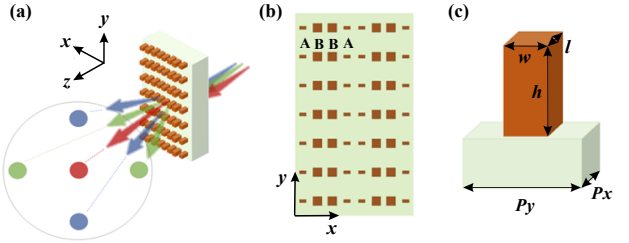


**Fig. 1.** (a) Schematic diagram of our proposed triple-band large-spatial separation beam splitter. The blue, green, and red arrows represent the blue, green, and red lights, respectively. (b) Top view of the metasurface, in which the meta-molecule has an arrangement of meta-atoms in A-B-B-A style. (c) Three-dimensional structure diagram of a single meta-atom.

Therefore, the normalized phase variation within the meta-molecule is $0 \sim (\pm\pi) \sim 0$. The mechanism of the $\pi$ phase shift along the $x$-direction comes from the size variation between meta-atoms A and B. On the other hand, in the $y$-direction, the meta-molecule has only one meta-atom. The phase of a blue light in a single meta-atom (either A or B) varies from $\varphi_{y0}$ on the upper boundary to $\varphi_{y0} \pm \pi$ in the center, and then back to $\varphi_{y0}$ on the lower boundary. Therefore, the normalized phase variation within the meta-molecule is $0 \sim (\pm\pi) \sim 0$. The mechanism of the $\pi$ phase shift along the $y$-direction comes from the resonance inside a single meta-atom. Besides, make sure that the phase-gradient is ignorable at red wavelengths so that the red light can pass directly through either A or B in both the $x$- and $y$-directions. In this way, the light at different bands of visible wavelengths can be steered to drastically different spatial positions. The blue light is split in the $y$-direction into two equal-intensity beams, the green light is split in the $x$-direction into another two equal-intensity beams, while the red light passes directly without splitting. The beam splitting angles in both the $x$- and $y$-directions obey the generalized Snell's law, and thus can be adjusted by the period of the meta-molecules.

The model was investigated by a three-dimensional finite-difference time-domain (3D FDTD) method using a commercial software (Lumerical 2019b FDTD Solver). In the simulation, the period of the meta-atoms along the $x$- and $y$-directions were $P_x = 250$ nm and $P_y = 500$ nm. In all-dielectric $TiO_2$ metasurfaces, achieving $2\pi$ phase coverage for a visible light requires a large meta-atom height, which was usually set to be 600 nm [31,37,40,41]. Such high $TiO_2$ nano-bricks can be fabricated by atomic layer deposition (ALD) and lift-off process [40,41]. Here, we discussed different heights ($h$) of the $TiO_2$ nano-bricks in the range from 450 to 550 nm, as well as different lengths ($l$) and widths ($w$) in the range from 50 to 200 nm, at different working wavelengths ($\lambda$) in the range from 400 to 780 nm. The optical constant of the $TiO_2$ material was taken from [42], while the refractive index of the $SiO_2$ material was 1.46. The $TiO_2$ nano-bricks were discretized using a grid mesh with $dx = dy = 5$ nm and $dz = 10$ nm, while the $SiO_2$ substrate and the air area were discretized automatically by the software. The periodic boundary condition was used in both the $x$- and $y$-direction s and the perfectly matched layer was applied in the $z$-direction.

## 3. RESULTS

### A. Size Optimization of Meta-Atoms

The key of our proposed beam splitter is to find the meta-atoms A and B. The phase diagram depends on both the size of the meta-atom and working wavelength.

Taking a small meta-atom with the size of $(h,\ l,\ w) = (450,\ 50,\ 50)$ nm and a large meta-atom with the size of $(h,\ l,\ w) = (550,\ 200,\ 200)$ nm as examples, the phase diagram of the blue (420 nm), green (530 nm), and red (730 nm) lights are illustrated in Fig. 2. At the 420 nm wavelength light, the phase along a straight line in the $y$-direction within a single meta-atom decreases from the upper boundary to the center and then increases from the center to the lower boundary, while the phase along a straight line in the $x$-direction within a single meta-atom is almost a constant. At the 530 nm or 730 nm

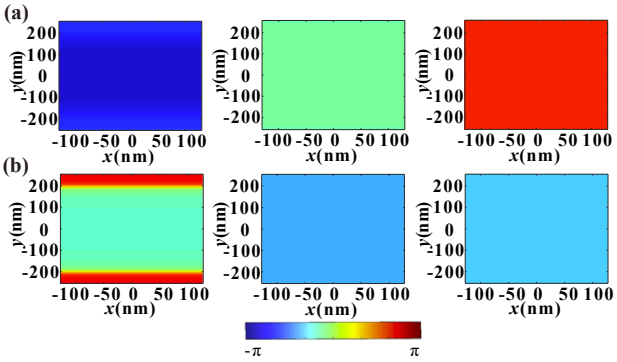


**Fig. 2.** Phase diagram of the 420 nm, 530 nm, and 730 nm wavelength lights after passing through (a) a small meta-atom with the size of $(h, l, w) = (450,\ 50,\ 50)$ nm and (b) a large meta-atom with the size of $(h, l, w) = (550,\ 200,\ 200)$ nm.

wavelength light, the phase within a single meta-atom is almost a constant.

As a consequence, for a given meta-atom at a fixed wavelength, we define $\varphi_x$ as the constant phase along the center line in the $x$-direction, $\varphi_{x0}$ as the value of $\varphi_x$ in the center, $\varphi_y$ as the variable phase along the center line in the $y$-direction, and $\delta\varphi_y$ as the difference of $\varphi_y$ between the center and the boundary. The optimized size of the meta-atoms can be determined based on their phase response of $\varphi_{x0}$ and $\delta\varphi_y$ given in Figs. 3–5, as well as their transmittance given in Fig. 6, if the triple-band central wavelengths are pre-designed as 420 nm, 530 nm, and 730 nm. According to the design principle described in Section 2, we should select two points in Figs. 3–5 to simultaneously satisfy Eqs. (1–3), where one point, $P_1$, with the size of $(h_1, l_1, w_1)$ is for the meta-atom A and another point, $P_2$, with the size of $(h_2, l_2, w_2)$ is for the meta-atom B. For the sake of easy fabrication, $h_1$ equals $h_2$. In Fig. 3, for the 420 nm wavelength light, $\varphi_{x0}$ and $\delta\varphi_y$ satisfy Eq. (1),

$$\begin{cases} \varphi_{x0}(P_1) - \varphi_{x0}(P_2) = 0 \\ \delta\varphi_y(P_1) = \pm\pi \\ \delta\varphi_y(P_2) = \pm\pi \end{cases}. \tag{1}$$

In Fig. 4, for the 530 nm wavelength light, $\varphi_{x0}$ and $\delta\varphi_y$ satisfy Eq. (2),

$$\begin{cases} \varphi_{x0}(P_1) - \varphi_{x0}(P_2) = \pm\pi \\ \delta\varphi_y(P_1) = 0 \\ \delta\varphi_y(P_2) = 0 \end{cases}. \tag{2}$$

In Fig. 5, for the 730 nm wavelength light, $\varphi_{x0}$ and $\delta\varphi_y$ satisfy Eq. (3),

$$\begin{cases} \varphi_{x0}(P_1) - \varphi_{x0}(P_2) = 0 \\ \delta\varphi_y(P_1) = 0 \\ \delta\varphi_y(P_2) = 0 \end{cases}. \tag{3}$$

In addition, both the two points should have a large transmittance in Fig. 6.

After careful selection, point $P_1(h_1, l_1, w_1) = (500, 120, 60)$ nm and point $P_2(h_2, l_2, w_2) = (500, 160, 160)$ nm can be selected for the meta-atoms A and B, respectively. The phase diagrams are similar to Fig. 2(b). At the 420 nm wavelength light, the normalized phase variation in the $y$-direction within the meta-molecule is nearly $0 \sim (-\pi) \sim 0$, while there is nearly no phase change in the $x$-direction within the meta-molecule. At the 530 nm wavelength light, the normalized phase variation in the $x$-direction within the meta-molecule is nearly $0 \sim (-\pi) \sim 0$, while there is nearly no phase change in the $y$-direction within the meta-molecule. At the 730 nm wavelength light, there are nearly no phase change in both the

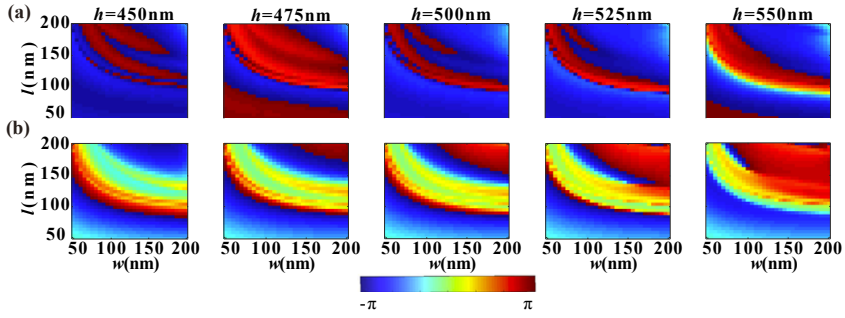


**Fig. 3.** (a) $\varphi_{x0}$ and (b) $\delta\varphi_y$ of the 420 nm wavelength light after passing through the meta-atom with various size.

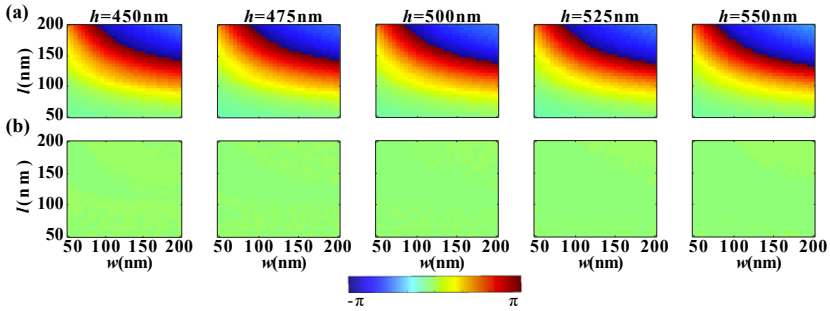


**Fig. 4.** (a) $\varphi_{x0}$ and (b) $\delta\varphi_y$ of the 530 nm wavelength light after passing through the meta-atom with various size.

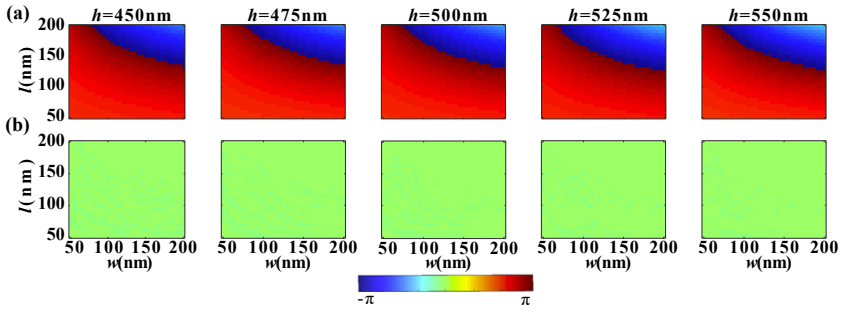


**Fig. 5.** (a) $\varphi_{x0}$ and (b) $\delta\varphi_y$ of the 730 nm wavelength light after passing through the meta-atom with various size.

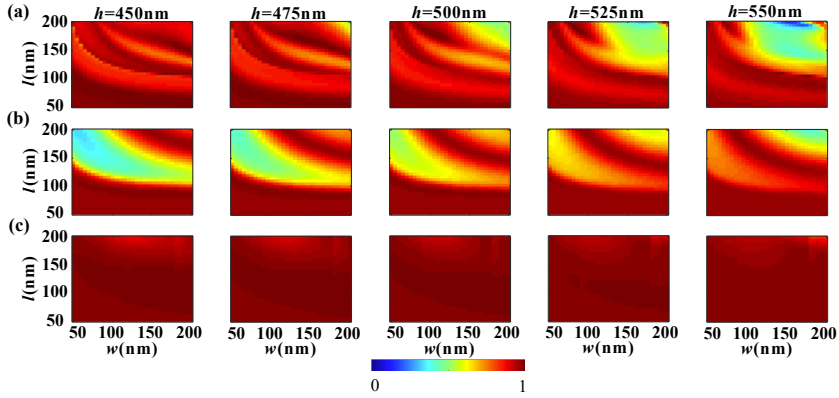


**Fig. 6.** Transmittance of the (a) 420 nm, (b) 530 nm, and (c) 730 nm wavelength lights after passing through the meta-atom with various size.

$x$- and $y$-directions within the meta-molecule. The transmittance of the meta-atoms A and B at the three pre-designed central wavelengths are higher than 0.8.

Finally, the whole metasurface composed of the optimized meta-atoms, shown in Fig. 1, was simulated. The far-field angle distribution of the electric field intensity and the cross-section of the electric field distribution of the transmitted lights are presented in Fig. 7. The 420 nm wavelength light is split in the $y$-direction into two equal-intensity beams, the 530 nm wavelength light is split in the $x$-direction into another two equal-intensity beams, and the 730 nm wavelength light passes directly without splitting, which are the same as the design. The beam splitting angles in the $x$- and $y$-directions are estimated

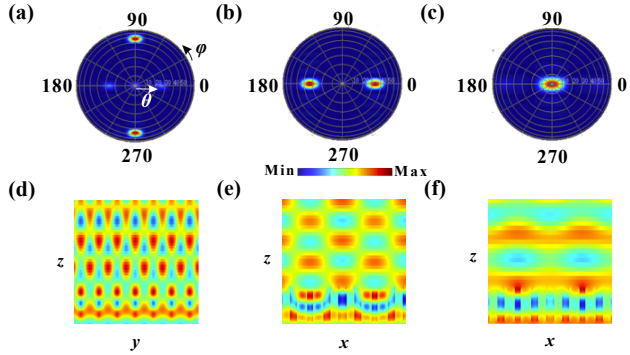


**Fig. 7.** Far-field angle distribution of the electric field intensity of the transmitted lights at the wavelengths of (a) 420 nm, (b) 530 nm, and (c) 730 nm. $\theta$ is the zenith angle and $\varphi$ is the azimuth angle. The cross-section of the electric field distribution of the transmitted lights at the wavelengths of (d) 420 nm, (e) 530 nm, and (f) 730 nm.

at about 32° and 57°, respectively, which coincide well with the theoretical values of 32.005° and 57.1401°, respectively, according to the generalized Snell's law.

### B. Working Efficiency

The working efficiency was defined as the ratio of the optical power in the desired spatial position to the optical power of the incident beam at a specific wavelength [23]. Therefore, the total working efficiency, $\eta_{\text{total}}$, can be defined as Eq. (4),

$$\eta_{\text{total}} = \begin{cases} \eta_t + \eta_b, & \text{for blue lights} \\ \eta_l + \eta_r, & \text{for green lights} \\ \eta_c, & \text{for red lights} \end{cases}, \tag{4}$$

where $\eta_t$ and $\eta_b$ are the working efficiencies of the top and bottom beam for blue lights, $\eta_l$ and $\eta_r$ are the working efficiencies of the left and right beam for green lights, and $\eta_c$ is the working efficiency of the center beam for red lights.

Figure 8 shows the normalized far-field intensity distributions along the center line in the dominant splitting direction. The three pre-designed wavelengths perform best in their respective band regions with regard to the far-field intensity. If the working wavelength deviates from the pre-designed central wavelength, then the deviation in the blue or green band would lead to the increment of the power allocation on the 0-th diffraction order and/or the decrement of the power allocation on the desired high diffraction order, while the deviation in the red band would lead to the opposite tendency. As a result, the 420 nm and 530 nm wavelength locate the peak of the total

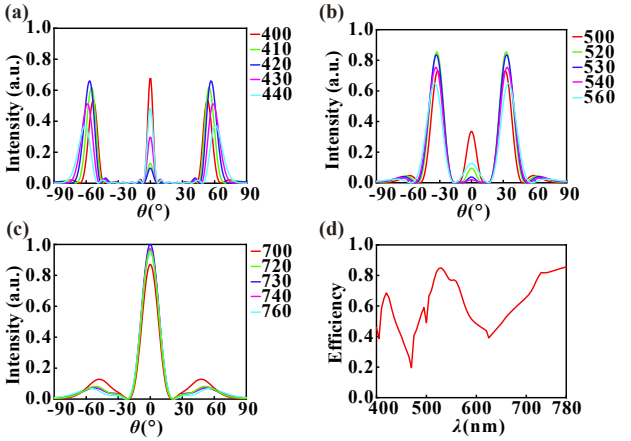


**Fig. 8.** Normalized far-field intensity distributions along the center line in (a) the $y$-direction for the blue band, (b) the $x$-direction for the green band, and (c) the $x$-direction for the red band. (d) The total working efficiencies of the triple-band beam splitter at visible wavelengths.

working efficiency curve in the blue and green bands, respectively, and the 730 nm wavelength also has good efficiency in the red band. Under normal incidence, the blue and green lights are split with equal intensity. The 420 nm wavelength light is split at the angle of about 57° in the $y$-direction with the total working efficiency of 68.1%, the 530 nm wavelength light is split at the angle of about 32° in the $x$-direction with the total working efficiency of 85.0%, and the 730 nm wavelength light passes directly at the angle of 0° with the total working efficiency of 81.9%. Compared to the recent published papers [23,24], the total working efficiencies of our proposed triple-band large-spatial-separation beam splitter are significantly improved.

Considering the fabrication tolerance, the working efficiency of the three wavelengths was discussed on condition that the size deviation, $\delta$, from the target value of $w$ or $l$ in the meta-atoms was from −20 to 20 nm. As shown in Fig. 9(a), the working efficiency of the 420 nm wavelength light decreases as $|\delta|$ increases, where $|\delta|$ is the absolute value of the size deviation. If $|\delta|$ is 10 nm (or 20 nm), then the working efficiency still remains above 60.5% (or 43.8%), which is 88.8% (or 64.4%) of the case without size deviation. Figures 9(b) and 9(c) indicate that the fluctuation of the working efficiencies for the 530 nm and 730 nm wavelength lights is much less than that for the 420 nm wavelength light, as $|\delta|$ increases. For the worst case with $|\delta|$ of 20 nm, the working efficiencies for the 530 nm and 730 nm wavelength lights remains higher than 71.3% and 72.2%, respectively, which reaches 83.9% and 88.2%, respectively, in the case without size deviation.

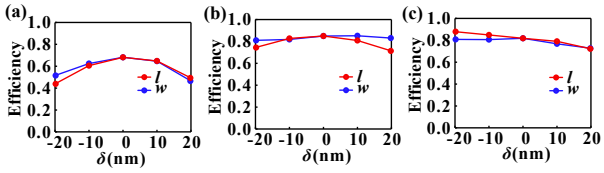


**Fig. 9.** Working efficiencies for (a) 420 nm, (b) 530 nm, and (c) 730 nm wavelength lights with different $\delta$, where $\delta$ is the deviation from the target value of $w$ or $l$ in the meta-atoms.

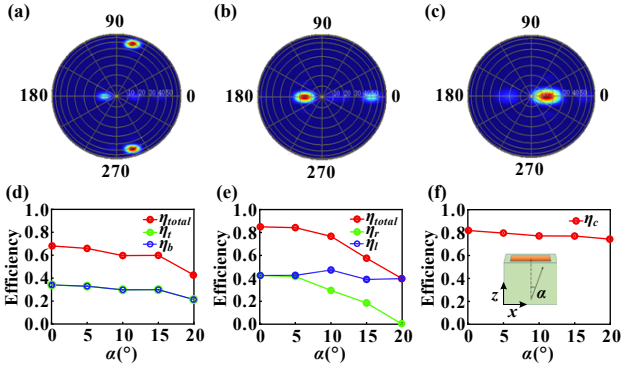


**Fig. 10.** Far-field angle distributions of the electric field intensity for (a) 420 nm, (b) 530 nm, and (c) 730 nm wavelength lights under the incident angle of 10° in the $x$-direction. The working efficiencies for (d) 420 nm, (e) 530 nm, and (f) 730 nm wavelength lights under different incident angles in the $x$-direction. The inset in (f) shows the inclined incident angle, $\alpha$, in the $x$-direction.

### C. Oblique Incidence

The performance of the triple-band beam splitters under oblique incidence with the inclined angle in the range from 5° to 20° were investigated.

If the incident light is inclined in the $x$-direction, as shown in Fig. 10, then the splitting beams would shift to the right side along the $x$-direction with lower working efficiencies compared to the normal incidence cases. For the 420 nm wavelength light, both $\eta_t$ and $\eta_b$ decrease with the same variation rate as the inclined angle increases, indicating that the splitting keeps equal intensity in the $y$-direction, although new diffraction orders appear in the center. For the 530 nm wavelength light, the energy is transferred from the right beam (the direction of movement) to the left beam, thereby the $\eta_r$ decreases very quickly as the inclined angle increases, and the $\eta_l$ has little variation, indicating an unequal intensity splitting in the $x$-direction. Moreover, the right beam disappears at the inclined angle of 20°, and then the beam splitter degenerates into a deflector. For the 730 nm wavelength light, the beam splitter represents as a deflector with a decreased $\eta_c$ as the inclined angle increases.

If the incident light is inclined in the $y$-direction, as shown in Fig. 11, then the splitting beams would shift to the top side along the $y$-direction with lower working efficiencies compared to the normal incidence cases. For the 420 nm wavelength light, the energy is transferred from the top beam (the direction of movement) to the bottom beam, thereby the splitting has an unequal intensity in the $y$-direction. Moreover, the top beam disappears at the inclined angle of 10°, and then the beam splitter degenerates into a deflector. For the 530 nm wavelength light, the splitting keeps equal intensity in the $x$-direction, although new diffraction orders appear. For the 730 nm wavelength light, the beam splitter represents as a deflector with a decreased $\eta_c$ as the inclined angle increases.

### D. Polarization Sensitivity

The polarization sensitivity of the triple-band beam splitter under normal incidence was also explored and presented in Fig. 12. When the polarization angle of the normal incident light is swept from 0°, which is the $x$-polarization, to 90°, which

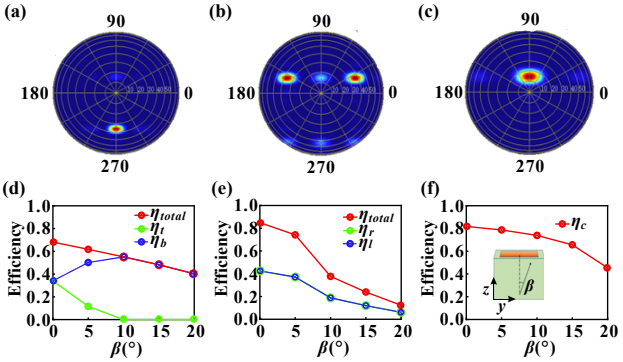


**Fig. 11.** Far-field angle distributions of the electric field intensity for (a) 420 nm, (b) 530 nm, and (c) 730 nm wavelength lights under the incident angle of 10° in the $y$-direction. The working efficiencies for (d) 420 nm, (e) 530 nm, and (f) 730 nm wavelength lights under different incident angles in the $y$-direction. The inset in (f) shows the inclined incident angle, $\beta$, in the $y$-direction.

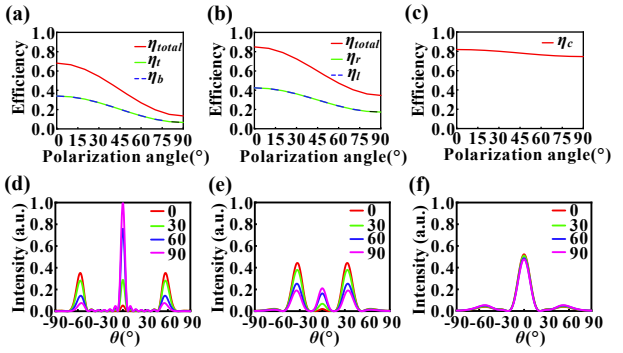


**Fig. 12.** Working efficiencies for (a) 420 nm, (b) 530 nm, and (c) 730 nm wavelength lights under normal incidence with different polarization angles. The normalized far-field intensity distributions along the center line in (d) the $y$-direction for 420 nm, (e) the $x$-direction for 530 nm, and (f) the $x$-direction for 730 nm under normal incidence with different polarization angles.

is the $y$-polarization, the working efficiencies severely decrease from 68.1% to 13.4% for the 420 nm wavelength light and from 85.0% to 34.6% for the 530 nm wavelength light. It is shown that the increment of the power allocation on the 0-th diffraction order induces the decrement of the power allocation on the desired high diffraction order. Because the 730 nm wavelength light is less affected by the meta-atoms, its working efficiency slightly decreases from 81.9% to 74.6% as the polarization angle increases.

## 4. CONCLUSION

A triple-band large-spatial-separation beam splitter was designed using a phase-gradient metasurface composed of $TiO_2$ nano-bricks. The three different wavelengths in the visible light bands have the same $x$-polarization and can be steered to drastically different spatial positions. Under normal incidence, the blue light is split in the $y$-direction into two equal-intensity beams, the green light is split in the $x$-direction into another two equal-intensity beams, while the red light passes directly without splitting. The mechanism of the $\pi$ phase shift along the $x$-direction for the green light comes from the size variation between adjacent meta-atoms, while the $\pi$ phase shift along the $y$-direction for the blue light comes from the resonance inside a single meta-atom. The optimized size of the meta-atoms was determined based on their phase response and transmittance. The beam splitting angles in both the $x$- and $y$-directions obey the generalized Snell's law. The working efficiencies under normal incidence are 68.1%, 85.0%, and 81.9% at the wavelengths of 420 nm, 530 nm, and 730 nm, respectively. If the incident light is inclined, then the beams would shift with lower working efficiencies compared to the normal incidence cases. The splitting beams in the inclined direction has an unequal intensity, and the beam splitter degenerates into a deflector at a large, inclined angle, while the splitting beams in the orthogonal direction keeps equal-intensity and the non-splitting beam in the central direction represents as deflection. If the normal incident light is swept from $x$-polarization to $y$-polarization, then the working efficiencies severely decrease for 420 and 530 nm wavelength lights, while the 730 nm wavelength light has slight decrements.

**Funding.** Natural Science Foundation of Guangdong Province (2018A030310373); State Key Laboratory of Applied Optics, Changchun Institute of Optics, Fine Mechanics and Physics, Chinese Academy of Sciences (SKLAO2022001A03).

**Disclosures.** The authors declare no conflicts of interest.

**Data availability.** Data underlying the results presented in this paper are not publicly available at this time but may be obtained from the authors upon reasonable request.

## REFERENCES

1. Z. Li, E. Palacios, S. Butun, and K. Aydin, "Visible-frequency metasurfaces for broadband anomalous reflection and high-efficiency spectrum splitting," Nano Lett. **15**, 1615–1621 (2015).
2. R. Ursin, F. Tiefenbacher, T. Schmitt-Manderbach, H. Weier, T. Scheidl, M. Lindenthal, B. Blauensteiner, T. Jennewein, J. Perdigues, P. Trojek, B. Öemer, M. Fürst, M. Meyenburg, J. Rarity, Z. Sodnik, C. Barbieri, H. Weinfurter, and A. Zeilinger, "Entanglement-based quantum communication over 144km," Nat. Phys. **3**, 481–486 (2007).
3. M. Malak, "Beyond interferometers based on silicon-air Bragg reflectors: Toward on-chip optical microinstruments–A review," IEEE J. Sel. Top. Quantum Electron. **21**, 49–60 (2015).
4. H. Fukuda, K. Yamada, T. Tsuchizawa, T. Watanabe, H. Shinojima, and S. I. Itabashi, "Ultrasmall polarization splitter based on silicon wire waveguides," Opt. Express **14**, 12401–12408 (2006).
5. J.-C. Song, W. K. Jung, N.-H. Kim, and K. M. Byun, "Plasmonic wavelength splitter based on a large-area dielectric grating and white light illumination," Opt. Lett. **37**, 3915–3917 (2012).
6. U. G. Yasa, M. Turduev, I. H. Giden, and H. Kurt, "High extinction ratio polarization beam splitter design by low-symmetric photonic crystals," J. Lightwave Technol. **35**, 1677–1683 (2017).
7. C. Huang, W. Pan, X. Ma, and X. Luo, "Multi-spectral metasurface for different functional control of reflection waves," Sci. Rep. **6**, 23291 (2016).
8. S. Liu, L. Zhang, Q. L. Yang, Q. Xu, Y. Yang, A. Noor, Q. Zhang, S. Iqbal, X. Wan, Z. Tian, W. X. Tang, Q. Cheng, J. G. Han, W. L. Zhang, and T. J. Cui, "Frequency-dependent dual-functional coding metasurfaces at terahertz frequencies," Adv. Opt. Mater. **4**, 1965–1973 (2016).
9. A. Forouzmand and H. Mosallaei, "Shared aperture antenna for simultaneous two-dimensional beam steering at near-infrared and visible," J. Nanophoton. **11**, 010501 (2017).

10. A. Forouzmand and H. Mosallaei, "Composite multilayer shared-aperture nanostructures: A functional multispectral control," ACS Photon. **5**, 1427–1439 (2018).
11. X. Wang, J. Ding, B. Zheng, S. An, G. Zhai, and H. Zhang, "Simultaneous realization of anomalous reflection and transmission at two frequencies using bi-functional metasurfaces," Sci. Rep. **8**, 1876 (2018).
12. J. Luan, L. Huang, Y. Ling, W. Liu, C. Ba, S. Li, and L. Min, "Dual-wavelength multifunctional metadevices based on modularization design by using indium-tin-oxide," Sci. Rep. **9**, 11 (2019).
13. H. Hasani, M. Tamagnone, S. Capdevila, C. F. Moldovan, P. Maoddi, A. M. Ionescu, C. Peixeiro, J. R. Mosig, A. K. Skrivervik, and J. Perruisseau-Carrier, "Tri-band, polarization-independent reflectarray at terahertz frequencies: design, fabrication, and measurement," IEEE Trans. Terahertz Sci. Technol. **6**, 268–277 (2016).
14. Y. Zhuang, G. Wang, J. Liang, and Q. Zhang, "Dual-band low-scattering metasurface based on combination of diffusion and absorption," IEEE Antennas Wireless Propag. Lett. **16**, 2606–2609 (2017).
15. Y. Zhuang, G. Wang, Q. Zhang, and C. Zhou, "Low-scattering tri-band metasurface using combination of diffusion, absorption and cancellation," IEEE Access **6**, 17306–17312 (2018).
16. M. Xin, R. Xie, G. Zhai, J. Gao, D. Zhang, X. Wang, S. An, B. Zheng, H. Zhang, and J. Ding, "Full control of dual-band vortex beams using a high-efficiency single-layer bi-spectral 2-bit coding metasurface," Opt. Express **28**, 17374–17383 (2020).
17. R. Xie, D. Zhang, X. Wang, S. An, B. Zheng, H. Zhang, G. Zhai, L. Li, and J. Ding, "Multichannel high-efficiency metasurfaces based on tri-band single-cell meta-atoms with independent complex-amplitude modulations," Adv. Photon. Res. **2**, 2100088 (2021).
18. Y.-W. Huang, W. T. Chen, W.-Y. Tsai, P. C. Wu, C.-M. Wang, G. Sun, and D. P. Tsai, "Aluminum plasmonic multicolor meta-hologram," Nano Lett. **15**, 3122–3127 (2015).
19. Z. Y. Li, E. Palacios, S. Butun, and K. Aydin, "Ultrawide angle, directional spectrum splitting with visible-frequency versatile metasurfaces," Adv. Opt. Mater. **4**, 953–958 (2016).
20. E. Arbabi, A. Arbabi, S. M. Kamali, Y. Horie, and A. Faraon, "Multiwavelength polarization-insensitive lenses based on dielectric metasurfaces with meta-molecules," Optica **3**, 628–633 (2016).
21. B. Wang, F. Dong, Q.-T. Li, D. Yang, C. Sun, J. Chen, Z. Song, L. Xu, W. Chu, Y.-F. Xiao, Q. Gong, and Y. Li, "Visible-frequency dielectric metasurfaces for multiwavelength achromatic and highly dispersive holograms," Nano Lett. **16**, 5235–5240 (2016).
22. K. Li, Y. Guo, M. Pu, X. Li, X. Ma, Z. Zhao, and X. Luo, "Dispersion controlling meta-lens at visible frequency," Opt. Express **25**, 21419–21427 (2017).
23. B. H. Chen, P. C. Wu, V.-C. Su, Y.-C. Lai, C. H. Chu, I. C. Lee, J.-W. Chen, Y. H. Chen, Y.-C. Lan, C.-H. Kuan, and D. P. Tsai, "GaN metalens for pixel-level full-color routing at visible light," Nano Lett. **17**, 6345–6352 (2017).
24. X. Zou, Y. Zhang, R. Lin, G. Gong, S. Wang, S. Zhu, and Z. Wang, "Pixel-level Bayer-type colour router based on metasurfaces," Nat. Commun. **13**, 3288 (2022).
25. S. Tang, F. Ding, T. Jiang, T. Cai, and H.-X. Xu, "Polarization-selective dual-wavelength gap-surface plasmon metasurfaces," Opt. Express **26**, 23760–23769 (2018).
26. R. A. Deshpande, F. Ding, and S. Bozhevolnyi, "Dual-band metasurfaces using multiple gap-surface plasmon resonances," ACS Appl. Mater. Interfaces **12**, 1250–1256 (2020).
27. C. Wan, R. Yang, Y. Shi, G. Zheng, and Z. Li, "Visible-frequency metagratings for light steering, beam splitting and absorption tunable functionality," Opt. Express **27**, 37318–37326 (2019).
28. J. Li, Y. He, H. Ye, T. Wu, Y. Liu, X. He, and J. Cheng, "High-efficiency, dual-band beam splitter based on an all-dielectric quasi-continuous metasurface," Materials **14**, 3184 (2021).
29. D. Zhang, M. Ren, W. Wu, N. Gao, X. Yu, W. Cai, X. Zhang, and J. Xu, "Nanoscale beam splitters based on gradient metasurfaces," Opt. Lett. **43**, 267–270 (2018).
30. G. Yoon, D. Lee, K. Nam, and J. Rho, "Geometric metasurface enabling polarization independent beam splitting," Sci. Rep. **8**, 9468 (2018).
31. J. Wang, Q. Jiang, and D. Z. Han, "Multi-channel beam splitters based on gradient metasurfaces," Results Phys. **24**, 104084 (2021).
32. T. J. Cui, M. Q. Qi, X. Wan, J. Zhao, and Q. Cheng, "Coding metamaterials, digital metamaterials and programmable metamaterials," Light Sci. Appl. **3**, e218 (2014).
33. S. Liu, T. J. Cui, Q. Xu, D. Bao, L. Du, X. Wan, W. X. Tang, C. Ouyang, X. Y. Zhou, H. Yuan, H. F. Ma, W. X. Jiang, J. Han, W. Zhang, and Q. Cheng, "Anisotropic coding metamaterials and their powerful manipulation of differently polarized terahertz waves," Light Sci. Appl. **5**, e16076 (2016).
34. L. Zhang, S. Liu, L. Li, and T. J. Cui, "Spin-controlled multiple pencil beams and vortex beams with different polarizations generated by Pancharatnam-Berry coding metasurfaces," ACS Appl. Mater. Interfaces **9**, 36447–36455 (2017).
35. X. Xing, Y. Li, Y. Lu, W. Zhang, X. Zhang, J. Han, and W. Zhang, "Terahertz metamaterial beam splitters based on untraditional coding scheme," Opt. Express **27**, A1627–A1635 (2019).
36. X. Zhang, R. Deng, F. Yang, C. Jiang, S. Xu, and M. Li, "Metasurface-based ultrathin beam splitter with variable split angle and power distribution," ACS Photon. **5**, 2997–3002 (2018).
37. A. Ozer, N. Yilmaz, H. Kocer, and H. Kurt, "Polarization-insensitive beam splitters using all-dielectric phase gradient metasurfaces at visible wavelengths," Opt. Lett. **43**, 4350–4353 (2018).
38. J. Li, H. Ye, T. Wu, Y. Liu, Z. Yu, Y. Wang, Y. Sun, and L. Yu, "Ultra-broadband large-angle beam splitter based on a homogeneous metasurface at visible wavelengths," Opt. Express **28**, 32226–32238 (2020).
39. N. Yu, P. Genevet, M. A. Kats, F. Aieta, J.-P. Tetienne, F. Capasso, and Z. Gaburro, "Light propagation with phase discontinuities: Generalized laws of reflection and refraction," Science **334**, 333–337 (2011).
40. M. Khorasaninejad, W. T. Chen, R. C. Devlin, J. Oh, A. Y. Zhu, and F. Capasso, "Metalenses at visible wavelengths: Diffraction-limited focusing and subwavelength resolution imaging," Science **352**, 1190–1194 (2016).
41. W. Zhu, R. Yang, G. Geng, Y. Fan, X. Guo, P. Li, Q. Fu, F. Zhang, C. Gu, and J. Li, "Titanium dioxide metasurface manipulating high-efficiency and broadband photonic spin Hall effect in visible regime," Nanophotonics **9**, 4327–4335 (2020).
42. M. Polyanskiy, "Refractive Index Database," RefractiveIndex.INFO, 2023, https://refractiveindex.info/.